Measuring the Electron Density Roughness of the D-Region Ionosphere

Marc A. Higginson-Rollins[1], **Morris B. Cohen**[1]

[1]School of Electrical and Computer Engineering, Georgia Institute of Technology, 777 Atlantic Drive NW, Atlanta, GA 30332

Key Points:

- A method for characterizing the horizontal and vertical electron density roughness of the D-region using LF/MF signals of opportunity is outlined.
- Field campaign data is used to investigate typical values of the horizontal and vertical roughness.
- The electron density roughness of the D-region is compared using a 25.2 kHz source and a 319 kHz source with similar paths.

Corresponding author: Marc Higginson-Rollins, mahr3@gatech.edu

Abstract

We present a method of characterizing the horizontal and vertical electron density roughness of the D-region ionosphere using Nationwide Differential GPS (NDGPS) transmitters as Low Frequency (LF; 30−300 kHz) and Medium Frequency (MF; 300−3000 kHz) signals of opportunity. The horizontal roughness is characterized using an amplitude cross-correlation method, which yields the correlation length scale metric. The vertical roughness is characterized using a differential phase height, which is needed to mitigate the effects of transmitter phase instability. The ranges and typical values of roughness metrics are investigated using data from several field campaign measurements. Finally, the roughness metrics for an NDGPS transmitter and VLF transmitter are compared. It is found that the roughness detected by the VLF transmitter is significantly smoother and demonstrates the utility of this method to complement traditional VLF measurements.

1 Introduction

The D-region of the ionosphere, which ranges from about 60-100 km, is too high for continuous in-situ measurements, such as with high-altitude balloons, and too low for satellite-based measurements. Molecular oxygen and nitrogen, nitric oxide, and other atoms, such as sodium and calcium, constitute this layer of ionization (Nicolet & Aikin, 1960). The ionization in the D-region of the ionosphere is primarily due to Lyman-α radiation during the day and cosmic rays and Lyman-β backscatter from the Earth's hydrogen exosphere at night (Kotovsky & Moore, 2016). This ionization acts as a dispersive, anisotropic media that reflects lower frequency waves and attenuates higher frequencies.

Since the D-region (and the ground) reflects lower frequency waves efficiently, the region between the Earth and the D-region is often referred to as the "Earth-Ionosphere Waveguide". An effective and widespread method to study the D-region is through the use of Very Low Frequency (VLF, 3−30 kHz) and Low Frequency (LF, 30−300 kHz) radio waves from man-made transmitters, (e.g. (Füllekrug et al., 2019)), or natural sources (e.g. (McCormick et al., 2018)), due to the efficient reflection of waves that allow propagation to global distances. As the frequency of the wave increase, the attenuation of the reflected signal increases as well, (Bickel, 1957), as does the reflection height. Waves between LF and Medium Frequencies (MF, 300−3000 kHz) reflect higher, with higher attenuation, but still reflect within the D-region and can serve to complement VLF observations. Waves around 200−400 kHz have previously been used to monitor and study the D-region, (Belrose et al., 1959; Bickel, 1957; Clarke, 1962; C. McKerrow, 1957; C. A. McKerrow, 1960; Belrose & Thomas, 1968). (Higginson-Rollins & Cohen, 2017) found that the United States Coast Guard's (USCG) Nationwide Differential Global Position System (NDGPS) can be used as a signal of opportunity for studying the D-region and captures perturbations typically associated with the D-region. (Higginson-Rollins & Cohen, 2020) used NDGPS transmitters to study the effect of the August 2017 "Great American" solar eclipse on D-region electron density.

The "small-scale roughness" of the electron density of the D-region is not well understood. The bulk of VLF research studying the D-region has been focused on global or regional studies, and typically all assume a stratified ionosphere. Some previous work done at VLF, e.g. (Lay & Shao, 2011b, 2011a; Füllekrug et al., 2015), examined more localized variation, but these studies are by no means exhaustive and fail to truly characterize roughness on a scale less than 10-100 km, particularly under ambient conditions. Early work done using the partial reflection technique touches on the idea of small-scale roughness, but the work was limited in scope and focused on understanding the mechanism of weak partial reflections rather than characterizing the roughness, e.g. (Shapiro, 1973), (Mathews et al., 1973), and (W. K. Hocking, 1979). This paper will outline a tech-

nique for studying the small-scale electron density roughness of the D-region using NDGPS transmitters. Metrics for determining the horizontal and vertical roughness will be described and applied to field campaign data.

2 Data Collection and Interpretation

2.1 LF AWESOME Receivers

The data in this paper was collected using the LF AWESOME Receiver (Cohen et al., 2018). This instrument consists of two orthogonal air-core loop antennas and has a sampling rate of 1 MHz, giving a band-pass of approximately 0.5−470 kHz, sensitivity up to 0.03 fT/$\sqrt{Hz}$ at 30 kHz and 0.1 fT/$sqrtHz$ at 300 kHz, and RMS timing accuracy of 15−20 ns for the RMS accuracy of all the timing pulses that make up the 1 MHz clock (implying precise phase estimation of <1.5 degrees at 300 kHz), there is no frequency drift/offset in the clock detectable with 0.5 part-per-billion resolution. The Georgia Tech Low Frequency Lab currently operates a network of 11 receivers throughout the United States and Japan. The two receivers used for this paper are located at: 1) Baxley, Georgia, [31.8767° N, 82.3621° W], 2) Pisgah Astronomical Research Institute (PARI), North Carolina, [35.1996° N, 82.8719° W].

2.2 NDGPS Transmitters

The NDGPS network consists of 33 sites which broadcast, between 285−325 kHz, the difference between a known, fixed location and the received GPS coordinates to improve the accuracy of commercial GPS to centimeter accuracy (D. Last & Poppe, 1996; J. Last & Poppe, 1997; Wolfe et al., 2000). From extensive measurements using multiple transmitters and receivers, it has been found that the transmitter clocks drift, which causes phase instability, limiting the usefulness of the phase data. Thus, in this paper, only amplitude metrics are considered. Three transmitters will be used for this paper: 1) New Bern, North Carolina, [35.1750° N, 77.0485° W], 2) Tampa, Florida, [27.8502° N, 82.5324° W], and 3) Bobo, Mississippi, [34.1152° N, 90.6912° W]. Respectively, the transmitters have a baud rate of 100 bits-per-second (BPS), 200 BPS, and 200 BPS, and a center frequency of 294 kHz, 312 kHz, and 297 kHz.

2.3 Data Interpretation

The receiver collects broadband data for both the North/South (N/S) and the East/West (E/W) channel. A synchronized minimum-shift keyed (MSK) demodulation is then applied to the broadband data, which converts the MSK modulated transmitter signal into a quasi-CW (continuous wave) signal. The result is that the horizontal magnetic flux density of a narrowband transmitter can be represented by the amplitude and (carrier) phase of the N/S and E/W channel. These four values can be written as two separate complex phasors that defines an ellipse centered at the origin. Measures can be derived from the resulting ellipse and include major axis length, minor axis length, right-hand circular polarization (RHCP), left-hand circular polarization (LHCP), ellipticity, tilt angle, and start phase. Synchronized MSK demodulation and the polarization ellipse method are both covered in great detail by (Gross et al., 2018). The work in this paper will primarily focus on the major axis length and the minor axis length. These parameters correspond to the transverse magnetic (TM) and transverse electric (TE) modes of the magnetic field respectively.

3 Characterizing Roughness

To determine the location and size of an active scattering region contributing to the total field at a receiving point from a surface illuminated by a source the commonly

accepted answer is the *Fresnel zones*, specifically the first Fresnel zone. At oblique incidence angles, such as in the case of a radio wave reflection from the lower ionosphere, this answer becomes less rigorous, but has been used in other works in this context, such as in (Lay & Shao, 2011b) and (Lay & Shao, 2011a).

The basic idea of the first Fresnel zone is as follows. Imagine a surface, such as the D-region, illuminated by a transmitter that in turn reflects radio waves, which are detected by a receiver at some distance. The locus of all points on the reflecting surface that generate a reflection that arrives at the receiver with a constant phase difference, δ, with respect to the direct radiation along d is given by Equation 1. In Equation 1, R_1 and R_2 are the distances of the up going and down going rays and δ is the constant phase difference. If δ is incremented in steps of $\frac{\lambda}{2}$, concentric ellipses with phase differences of π will arise. This effectively creates rings of alternating constructive and destructive phase interference, which form ellipses on the D-region, where the first Fresnel zone will be defined as the area inside the first ellipse where the locus of all points will constructively interfere with a phase of π. In general, the first Fresnel zone, or the first ellipse on the surface, has the greatest contribution to the received signal because of the following reasons: 1) the concentric ellipses, after the first Fresnel zone, have a decreasing area and thus decreasing contribution to the received signal, 2) the alternating concentric ellipses of constructive and destructive interference, though not identical in size, approximately cancel out. For a thorough reference text on Fresnel zones and related topics refer to (P. Beckmann & A. Spizzichino, 1963).

$$R_1 + R_2 - d = \delta \tag{1}$$

In the case of a receiver detecting the signal from an LF/MF transmitter, such as an NDGPS transmitter, at oblique incidences, the first Fresnel ellipse will appear as an ellipse that becomes more elongated as the distance between the transmitter and receiver increases. The direction along the path of propagation, or rather the direction towards the receiver from the transmitter, is called the *radial* direction. The direction perpendicular to the direction of propagation is called the *transverse* direction. The radial and transverse first Fresnel radii can be calculated for varying propagation distances. For example, assume a propagating wave has a frequency of 300 kHz, a reflection height of 90 km, and a propagation distance of 600 km. The radial radius would be about 43.2 km and the transverse radius would be 12.5 km. If the propagation distance is increased to 1200 km, the radial radius would increase to about 115.3 km and the transverse radius would increase to 17.4 km. Thus, the active scattering region, i.e. the first Fresnel zone, grows with distance and can become quite large at longer distances. It should also be noted that, at distances of about 700−1200 km, the first skywave is the dominant mode. This means that, at these distances, the first Fresnel zone is effectively a "patch" of the D-region that is being probed by the LF/MF waves with minimal contributions from higher order modes. The metrics discussed in the next sections will focus on describing the "vertical" and "horizontal" roughness of the D-region by exploiting this concept, specifically that the patch of the D-region being probed is more or less equivalent to the Fresnel zone at the center of the propagation path between the transmitter and receiver.

The remainder of this section outlines the two key metrics that will be used to measure the roughness of the D-region electron density in terms of the vertical, differential phase height, and horizontal roughness, correlation length scale. Both these metrics exploit the concept of the first Fresnel zone, which is the patch that is being probed by the transmitter.

3.1 Vertical Roughness

A group of methods used to estimate the reflection height of a low frequency wave from the D-region using phase data are called *virtual reflection height* methods. A summary of these methods can be found in (Piggott et al., 1965). This section will focus on one method in particular called the *phase height* method and is described by h_1 in Equation 2, where λ is the wavelength, I is the angle of incidence from the vertical plane pointed from the ground to the ionosphere, θ_g is the phase difference between the up-going and down-coming waves observed at the ground, and M is simply an arbitrary integer. It is import to note, that the solution of Equation 2 is not unique and is dependent on the choice of M.

$$\frac{-4\pi h_1}{\lambda}\cos I = (2M+1)\pi + \theta_g \tag{2}$$

However, the NDGPS transmitters being used as a signal of opportunity suffer from clock instabilities that cause ramping in the phase data. This is problematic since the possible equivalent reflection height techniques from (Piggott et al., 1965) are all reliant on phase data. To cope with this problem, a modification has been made to the *phase height* technique described in Equation 2. First, envision a propagation scheme, like the one depicted in Figure 1, where a transmitter, left, is detected by two receivers, right, at some distance d_1 and d_2 away. Each wave, depicted in the figure as a ray, propagates in a similar path and reflects off the D-region, seen as the blue region above, at some height, h_1 and h_2 respectively, with some angle of incidence, θ_1 and θ_2. An important assumption made here is that the receivers are placed sufficiently far from the transmitter, e.g. approximately 700 km to 1200 km, in order to ensure that only one skywave is propagating.

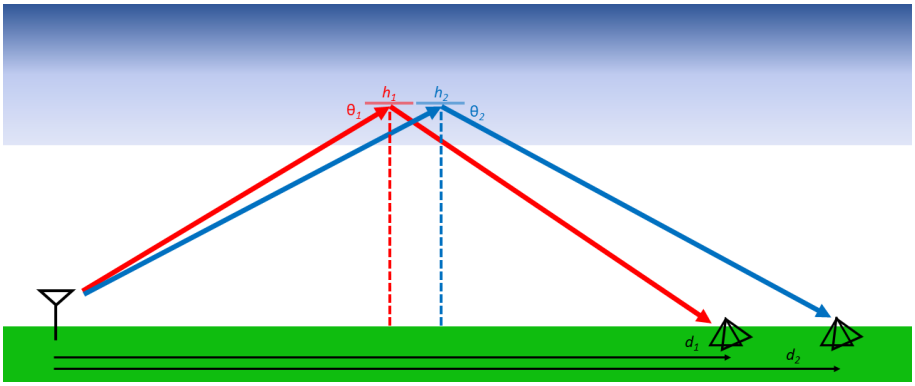

Figure 1. Example propagation scheme of a transmitter (left) and two closely spaced receivers (right) with the waves reflecting off of the D-region.

With two receivers, there are now phase measurements at two different locations. This will be the key difference between the *phase height* method described in Equation 2 and what will now be called the *differential phase height*. Equation 3 describes what happens when the two phase values at each receiver, ϕ_1 and ϕ_2, are subtracted from each other. Each phase value can be broken into three parts: 1) the contribution of the transmitter source ($\phi_{n,source}$), 2) the ionospheric and path contribution ($\phi_{n,ionosphere}$), and 3) the contribution from nearby scattering ($\phi_{n,site}$). Between the two receivers, the contribution from the transmitter source should be identical and thus, when subtracted, should cancel completely, which effectively eliminates the "phase ramping" described above. The remaining phase elements are described in Equation 4, where $\phi_{\Delta,ionosphere}$ is the differ-

ence in the ionospheric, and path, contribution, ϕ_{noise} is the contribution of any time varying noise (e.g. receiver noise), and ϕ_{bias} is the contribution of any "constant bias", such as nearby scattering from geographical features or buildings.

$$\phi_\Delta = \phi_1 - \phi_2 = \phi_{1,source} + \phi_{1,ionosphere} + \phi_{1,site} - \phi_{2,source} + \phi_{2,ionosphere} + \phi_{2,site} \quad (3)$$

$$\phi_\Delta = \phi_{\Delta,ionosphere} + \phi_{noise} + \phi_{bias} \quad (4)$$

In Equation 2, the right-hand side can be encased into a variable, such as Equation 5. Given the right selection of M, the phase values from Equation 4 and Equation 5 will be equal, $\phi_\Delta = \phi'_\Delta$.

$$\phi'_\Delta = (2M+1)\pi + \theta_g \quad (5)$$

Thus, we can then substitute Equation 4 into Equation 2 and solve for the equivalent reflection height, yielding Equation 6. Where λ is the wavelength, θ_i is the angle of incidence (in radians), and ϕ_Δ is the phase from Equation 4.

$$H = -\frac{\phi_\Delta \lambda}{4\pi \cos\theta_i} \quad (6)$$

Next, the metric we are interested in is a *relative change* in phase height, rather than an absolute metric. Thus, the mean phase height, $\bar{H}$, is subtracted, which yields a normalized relative phase height, Δh, as in Equation 7. It should be noted that because of this normalization, the integer choice, M, from Equation 5 becomes irrelevant. This normalized, differential phase height is the final metric of interest. However, to measure its variation, the *root-mean-squared* of a subset time series of normalized differential phase height values is calculated, using Equation 8, to measure the vertical variation in the D-region.

$$\Delta h = H - \bar{H} \quad (7)$$

$$\sigma_{RMS} = \sqrt{\frac{1}{N}\sum_{n=1}^{N} |\Delta h|^2} \quad (8)$$

The values for the wavelength, λ, and phase, ϕ_Δ, are known, however, the angle of incidence, θ_i, is still an unknown. Assuming a spherical Earth, a formula for the angle of incidence based on the geometry of the problem can easily be solved using Equation 9, where R_e is the radius of the earth in meters, h_n is the reflection height in meters, and d_n is the distance from the transmitter to the receiver in meters. The subscript n indicates the receiver number. The resulting angle of incidence, $\theta_{i,n}$, is in radians. The formula on the right hand side is the angle from the vertical axis, the complementary angle of the angle of interest. Thus, the angle is subtracted from $\frac{\pi}{2}$, which yields an angle of incidence that can be used in Equation 6.

$$\theta_{i,n} = \frac{\pi}{2} - \arctan\frac{R_e \sin\frac{d_n}{2R_e}}{h_n + R_e(1-\cos\frac{d_n}{2R_e})} \quad (9)$$

In Equation 9, there is still one unknown: the reflection height, h_n. However, only the *relative change* in this variable is of interest. Thus, a best guess value for h_n is used and left constant. This approximation results in a small error that decreases as propagation distance increases. For example, if the reflection height is assumed to be 90 km with a nighttime range of reflection heights of $85 - 95$ km for a wave at 300 kHz. For a propagation range of 900 km the error, that is the difference between the chosen value and the bounds, is $\theta_{error,i} \approx \pm 0.6°$.

An additional consideration for the use of Equation 6 is that, although there is only one angle of incidence in the formula, there are actually two angles of incidence for the two receivers being used. Two possible solutions to this problem are: 1) to take the mean value of the two angles of incidence, 2) to pick one angle of incidence and use it. In the context of this problem, the receiver spacing is often quite small, $< 10\lambda$, and if it's chosen to be closer to $\approx \lambda$, then the error in the angle of incidence, if only a fixed value is used, drops drastically. At a propagation distance of 900 km, the difference between two receivers spaced one wavelength apart, with identical reflection heights, is only $\theta_{error,i} \approx 0.01°$. Thus, this error becomes negligible under the right circumstances.

In conclusion, to measure the vertical roughness, or variability, of the D-region the *differential phase height* method described above will be used to track the relative change in phase height. Equation 6 is used to calculate the differential phase height using a fixed value of angle of incidence, calculated using Equation 9, where an initial reflection height of 90 km is used and kept constant. The resulting value is normalized using Equation 7 and then the root-mean-squared value is calculated form a subset of the time series using Equation 8. The final metric describes the variability in the vertical phase height between two "patches", Fresnel zones, reflecting off the D-region.

3.2 Horizontal Roughness

The second component of characterizing the electromagnetic roughness of a surface is determining the "horizontal roughness". A common technique for characterizing spatial variability, which can be applied to this problem, is called *cross-correlation analysis*. Variants of this method are widely used to solve problems in different remote sensing fields. The work by (J. Doviak et al., 1994), and citations within, used spaced receiver models and cross-correlation analysis to study atmospheric turbulence and wind parameters. A paper by E. N. Bramley, (Bramley, 1951), similar to the paper by (Briggs et al., 1950), summarizes the use of a cross-correlation analysis technique on the reception of radio waves from the ionosphere for two closely spaced aerial antennas, such as two antennas on an airplane, for various conditions, such as whether there is a steady signal present or not. This work was expanded on by (Lindner, 1975b) and (Lindner, 1975a) to, using the partial reflection technique, understand the angular spread of down coming reflected waves, the coherence ratio, and the scale/size of reflecting ionospheric irregularities. The work by (Wernik et al., 1983) used spaced receivers to study turbulent ionospheric irregularities, specifically the mean drift velocity and direction, the characteristic random velocity, the spatial scales of the irregularities, and the orientation of the irregularities. Cross-correlation analysis has been successfully used in similar remote sensing fields and can be applied to measure the spatial roughness of the D-region electron density.

The primary metric derived from cross-correlation analysis is the *correlation length scale*. The correlation length scale is a statistical measure that describes the spatial variance of a surface. In the context of this work, the correlation length scale will be used to measure the spatial variance in the amplitude of a wave reflecting from the ionosphere.

It is well established in literature that the correlation length scale measured on the ground can be used as a proxy for the scale of a perturbation or to estimate the angular spread of the scattering from a surface, (Ratcliffe, 1956). When the ionosphere is smooth,

the reflection will be *specular* and remain a narrow beam. As the roughness increases, the down coming ray becomes more diffuse and becomes a wider "cone" instead of a narrow beam. Thus, as the roughness of the surface increases in relation to the wavelength being used, the measured correlation length scale of should increase as well.

The correlation length scale is calculated as follows. First, the simultaneous amplitude data being analyzed (e.g. N/S amplitude, E/W amplitude, major axis length, or minor axis length) from multiple receivers is aggregated, such as in Equation 10, where each variable represents the time series of the metric being analyzed. In this case, the time series may be the complete time series of the data collected during the campaign or a windowed subset of it.

$$\vec{x} = [x_1(t), x_2(t), ..., x_d(t)] \tag{10}$$

Once the data has been aggregated, the data from each receiver is normalized individually by calculating the *Z-score*, Equation 11, where μ_x is the mean and σ_x is the standard deviation.

$$\bar{x} = \frac{x - \mu_x}{\sigma_x} \tag{11}$$

Using the normalized values, the cross-correlation is calculated between each pair of receiver metrics using Equation 12. Where x_{n+m} is one receiver site metric at time $t = n + m$ and y^*_m is the complex conjugate of the other receiver site metric at time $t = m$. The result from Equation 12 is then normalized using Equation 13.

$$\hat{R}_{xy}(m) = \begin{cases} \sum_{n=0}^{N-m-1} x_{n+m} y^*_n, & m \geq 0, \\ \hat{R}^*_{yx}(-m), & m < 0. \end{cases} \tag{12}$$

$$\hat{R}_{xy,coeff}(m) = \frac{1}{\sqrt{\hat{R}_{xx}(0)\hat{R}_{yy}(0)}} \hat{R}_{xy}(m) \tag{13}$$

The result of this calculation is used to find the *maximum* value of the *absolute* value of each receiver pair combination. This results in a diagonal matrix of size $D \times D$ where the diagonal values are equal to approximately 1. Each point in this matrix corresponds to a specific receiver spacing. Figure 2 illustrates the receiver spacing configuration for a radial propagation scheme. A transmitter, on the left, is transmitting a wave that reflects off the ionosphere, middle of figure, and is detected by some number of receivers, on the right. The receivers are located at a distance, $d_{1,2,...}$, from the transmitter. The spacing between the receivers can be calculated in two ways: 1) the spacing between the midpoints of the propagation paths, L', or 2) the ground spacing, L. Each element of the calculated diagonal matrix above has an equivalent diagonal matrix with elements corresponding to the spacing using either L' or L. For this work, the ground spacing of the receivers, L, is exclusively used in order to match the simulated results in the next section.

In general, the exact cross-correlation point is not captured, so an exponential fit, like the one in Equation 14, is used to approximate it. In Equation 14, "A" and "B" are coefficients and generally $A \approx 1$. Figure 3 shows an example of this process. The left panel shows the major axis, or H_ϕ, correlation length scale. The blue square points are cross-correlation values for each pair of receivers. The black line is the exponential fit for the blue squares and the red horizontal line is the e^{-1} point. The point at which these two lines intersect is the correlation length scale. The same plot is shown in the right panel for the minor axis, H_θ.

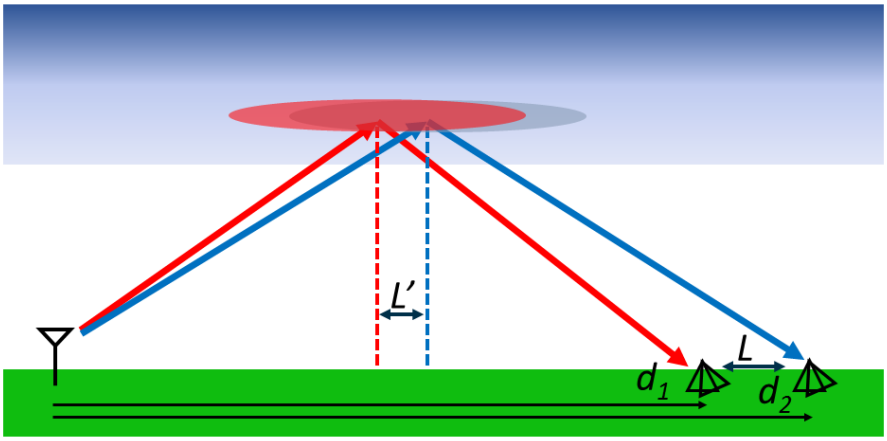

Figure 2. Example propagation scheme of a transmitter (left) and two closely spaced receivers (right) with the waves reflecting off of the D-region.

$$\hat{R}'(x) = A \exp^{Bx} \tag{14}$$

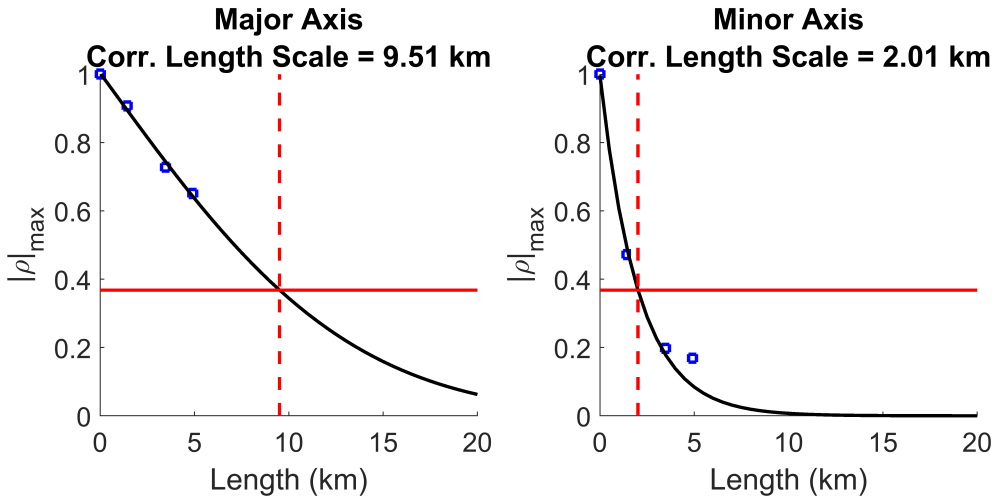

Figure 3. Example of estimating the correlation length scale using an exponential fit. The left panel shows the major axis cross-correlation values and the minor axis shows the minor axis values.

4 Field Campaign Data Analysis

With the two roughness metrics identified, the correlation length scale and the RMS height variation, field campaign data was collected. The collected field campaign data will be presented below. The roughness metrics will be applied to the data and discussed. Finally, comparisons will be made to VLF transmitters.

4.1 Field Campaigns

The D-region is non-stationary and fluctuates on a very quick timescale at nighttime, e.g. 5−25 minutes. Early partial reflection measurements had difficulty dealing with this issue when using amplitude statistics to study D-region scattering, (W. Hocking, 1987). Thus, receiver spacing and geometry, i.e. simultaneous spatial sampling of the ionosphere, will be critical in accurately measuring the roughness of the D-region. Two primary considerations will have to be taken into account: 1) measurements should be oriented transverse or radial to the propagation path with little deviation, 2) the transmitter-receiver propagation distances should be limited to approximately 600−1200 km to fall in the propagation region dominated by the first skywave.

Several field measurements were made over the course of 2019. In each field campaign, some number of mobile receivers were deployed sequentially in a predetermined location, with permission from the property owner, such as a farm, and data was collected for some period. The data collected at each site is truncated to maximize the simultaneous data. Table 2 summarizes the completed field campaigns, where spacing from reference indicates the distance from a chosen reference site. All the field campaigns were conducted near the permanent receiver site located at Baxley, Georgia, [31.8767° N, 82.3620° W] indicated by the blue dot in Figure 4. This site is located at the "bottom" of what is called the *Southeast Array*, indicated by the black dots in the figure. The red dots in Figure 4 indicate the location of each transmitter used for this work. The red lines show the great circle paths (GCP) from the transmitter to the permanent receiver site in Baxley (GA). Table 1 summarizes the red transmitter-receiver paths shown in the figure, where the distances listed are from the transmitter to the permanent Baxley (GA) receiver. The receivers were arranged in a predominantly North-South orientation to capture data from several transmitters in a combination of "radial" and "transverse" paths, as depicted in Figure 5 where the arrow indicates the direction towards the transmitter being detected.

Table 1. Summary of the transmitters and transmitter-receiver path geometries from the completed field campaigns.

Transmitter	Coordinates	Frequency (kHz)	Distance (km)	Orientation
Detroit (MI)	42.2972°N, 83.0952° W	319	1158.3	Radial
English Turn (LA)	29.8783°N, 89.9417° W	293	757.7	Transverse
Tampa (FL)	27.8502°N, 82.5325° W	312	446.6	Radial
Card Sound (FL)	25.4317°N, 80.4663° W	314	737.9	Radial

Table 2. Summary of the field campaigns conducted in 2019 where the spacing from reference is the distance between each receiver site from a fixed reference and the total time refers to the total time of simultaneous data collection.

Date	Number of Receivers	Spacing from Reference (km)	Total Time (Hours)
01/14/19	3	2.5, 5	0.777
01/14/19	3	5, 10	0.540
06/13/19	3	2.5, 5	0.432
06/13/19	3	2.5, 1.4	0.684
08/22/19	4	7.2, 1.4, 4.9	1.504
09/06/19	3	1.4, 4.9	3.983
09/07/19	5	7.3, 8.3, 8.6, 12	5.893

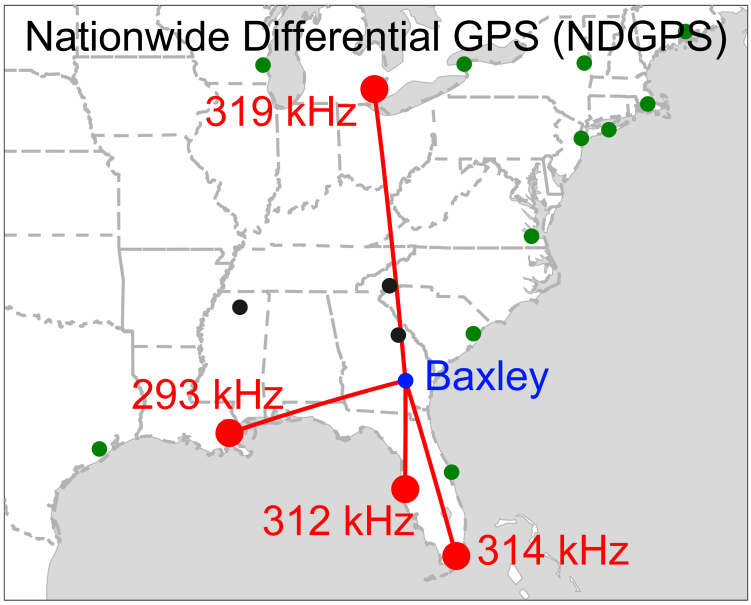

Figure 4. Map showing the transmitter-receiver paths for the completed campaigns. The receiver site is indicated by the blue dot and label. The transmitters are shown using the red dots, annotated with the respective transmission frequency.

4.2 Accounting for D-Region Non-Stationarity

In order to discern variations and trends in the measured D-region roughness metrics, the time series of all the data collected must be subsampled into smaller windows to increase the number of available observations. The optimal window size is one that has the smallest possible size, while maintaining stable stochastic properties. The first check is to test the stationarity of the process being detected. Stationarity is often an underlying assumption in time series analysis and enables the use of many simplifications. The two most common types of stationarity are: 1) *Strict-Sense Stationary* (SSS) and 2) *Wide-Sense Stationary* (WSS), see (Durgin, 2002). Unfortunately, it was found that the data collected from the data campaigns is not WSS, and thus not SSS, which aligns with literature since it is well known that the nighttime D-region is highly erratic, e.g. (Thomson et al., 2007). However, a meaningful method is needed to determine an (approximately) optimal window size to use to segment the data collected from the field campaigns. The work by (Arikan & Erol, 1998) discusses methods for determining a proper window size for sliding window statistics where the process will be "locally stationary", specifically in the context of ionospheric remote sensing. An empirical method described in this work is to inspect the data around the calculated sliding window mean, μ, for different window sizes and select the longest window for which most of the data lies within a standard deviation, σ, of the mean.

Analogous to above, increasing the window size used for a cross-correlation, the metric of interest, would increase its fidelity, but decrease its sensitivity to temporal variations. Thus, a proper window size would be as long as possible, while maintaining temporal sensitivity. This can be empirically found as the shortest window size that just stabilizes the variation in the correlation length scale. Figure 6 shows the change in correlation length scale as a function of time and window size. The top panel shows the major axis correlation length, where each line represents a different window size as noted in the legend. The red dashed line is the correlation length for the entire time series. Each point in each line corresponds to the start time of the window used. The bottom panel

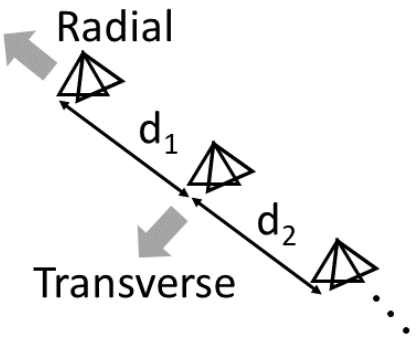

Figure 5. Orientation reference for the spaced receivers where the arrow indicates the direction towards the transmitter being detected.

shows the minor axis correlation length. It is evident from the figure that the correlation length scales in both the major and minor axis begin to converge around 25 minutes. Window overlapping can also be used in order to maximize the length of each window and the number of windows. Ultimately, a window size of 20 minutes with a 2.5-minute overlap (on each end) is used.

4.3 Roughness Metrics

Using a window and overlap size of 20 $\pm$ 2.5 minutes, as determined in the previous section, all the collected field campaign data can be segmented and analyzed. This section will focus on the "horizontal roughness", namely the correlation length scale. Figure 7 summarizes all the collected field campaign data. The data is segmented by major and minor axis and by the orientation of the antenna array in regard to the transmitter being detected. Recall that "radial" refers to the array being parallel to the path of propagation and "transverse" refers to the array being perpendicular to the path of propagation. In each of the four panels a histogram of the correlation length scale, normalized by the wavenumber according to Equation 15, is shown with the y-axis indicating the probability density function, or PDF. The geometric mean and standard deviation are shown in the top right corner of each panel. The black line over each histogram is a best fit Rician distribution meant to capture the shape and trend of the distribution of each data set. The most pronounced trend in the figure is the difference between the major and minor axis correlation lengths in terms of the shapes, i.e. mean and standard deviation, of the distributions. The differences between the radial and transverse distributions, for both the major and minor axis, are a lot more subtle. This may suggest that the major axis, or H_ϕ, is sensitive to a different scattering mechanism than the minor axis, or H_θ.

$$kL = \frac{2\pi}{\lambda} L \tag{15}$$

Another way of interpreting the data in Figure 7 is in reference to the estimated Fresnel zone size for the respective dimension. Figure 8 shows the same data as in Figure 7, but normalized by the Fresnel zone. Due to the long propagation paths used, the radial dimension of the Fresnel zone is much larger than the transverse dimension, with the latter remaining consistent. This property can be observed in the two left panels of the figure, the radial orientations, which have different shapes than those in Figure 7, but the right panels, the transverse orientation, remained fairly consistent. In literature,

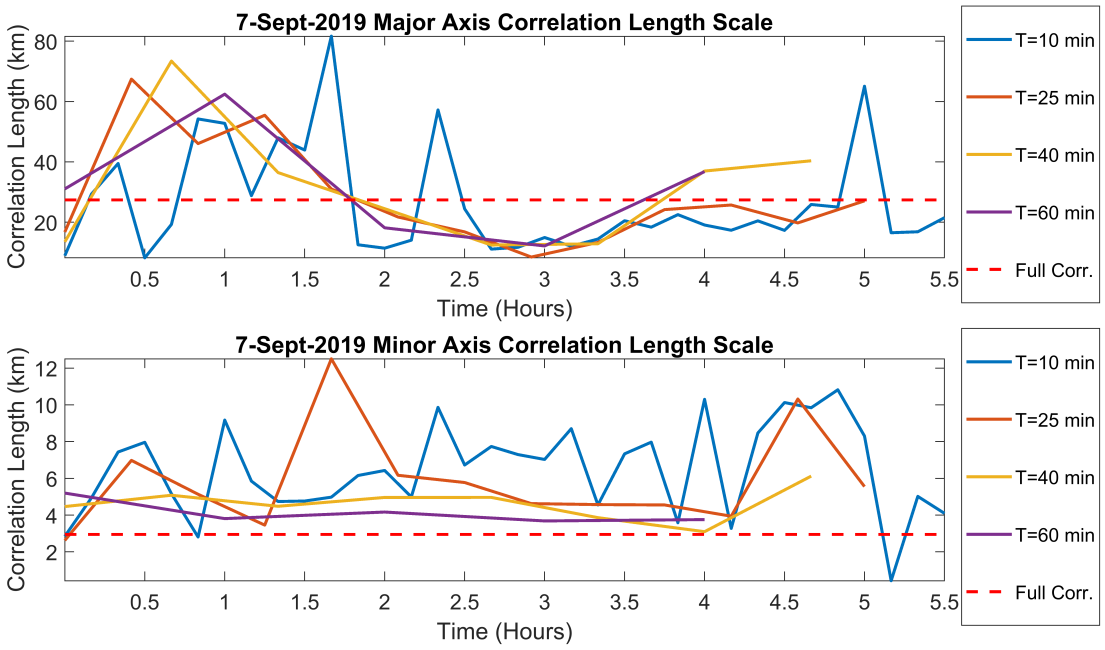

Figure 6. Superposition of the correlation length scale, as a function of time, calculated for varying window sizes. The top panel shows the major axis correlation length and the bottom panel shows the minor axis correlation length.

the ratio of the correlation length and the Fresnel zone is used to determine what, if any, approximations can be made to model scattering. The work done by (Spetzler & Snieder, 2001b), (Spetzler & Snieder, 2001a), and (Spetzler et al., 2002) investigated when it was appropriate to use ray theory versus scattering theory based on this ratio, which can be used to provide a sense of scale of roughness. The correlation length scale can be thought of as a proxy for the scale of the perturbation, (Bowles et al., 1963), or rather the resulting angular spreading of the signal, (Bramley, 1951) and (Lindner, 1975a). If the primary scattering mechanism is attributed to some number of small irregularities, then the correlation length scale is expected to be smaller than the Fresnel zone, (R. J. Doviak & Zrnic, 1983). If the correlation length scale is larger than the Fresnel zone, then it is suggested that a larger-scale structure is causing the scattering. The radial major axis, top left panel, and minor axis values, two bottom panels, both fall in the regime of "scattering theory", i.e. $\frac{L}{L_F} < 1$, while the top right panel, the case of the transverse major axis, falls partly in the regime of "ray theory", i.e. $\frac{L}{L_F} >> 1$.

Once more using the window size and overlap of 20±2.5 minutes, the data is segmented and analyzed to investigate the vertical roughness. Figure 9 summarizes all the collected field campaign data. The data is segmented by the orientation of the antenna array in regard to the transmitter being detected – radial and transverse. In each panel a histogram of the RMS height variation, normalized by the wavenumber according to Equation 16, is shown with the y-axis indicating the probability density function, or PDF. The geometric mean and standard deviation are shown in the top right corner of each panel. The black line over each histogram is a best fit Rician distribution meant to capture the shape and trend of the distribution of each data set. Unlike the correlation length scale data, the variation in the RMS height appears to be a lot lower. In addition, the RMS height appears to be consistent across field campaigns, however, as in the case of

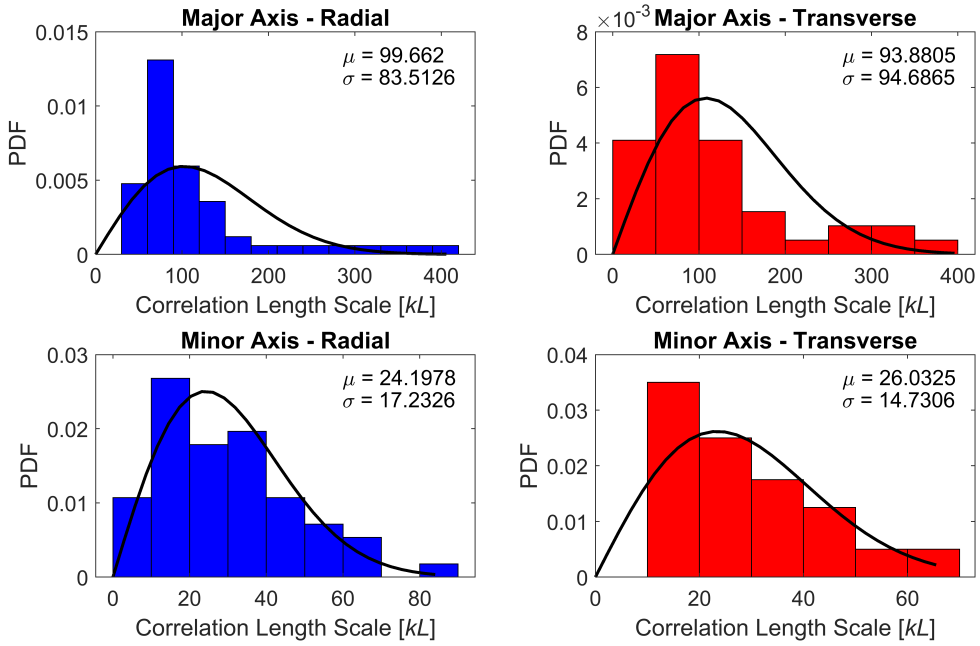

Figure 7. Summary of the measured correlation length scale values for all field campaigns. Top left panel: Major axis correlation length scale for the radial direction. Top right panel: Major axis correlation length scale for the transverse direction. Bottom left panel: Minor axis correlation length scale for the radial direction. Bottom right panel: Minor axis correlation length scale for the transverse direction.

the correlation length scale, more data must be collected in order to determine any seasonal trends.

$$k\sigma = \frac{2\pi}{\lambda}\sigma \tag{16}$$

4.4 Comparison to VLF Transmitters

Using a Very Low Frequency (VLF) transmitter on a similar path to a LF/MF NDGPS transmitter, the above roughness metrics can be studied as a function of frequency. This comparison can be done using the data collected on the 7-September-2019 field campaign in Baxley, Georgia, for the VLF transmitter in North Dakota, call sign "NML", and the NDGPS transmitter in Detroit, Michigan. Figure 10 shows the transmitter-receiver geometry (red lines) between Baxley, Georgia, (blue dot) and the two transmitters (red dots). The Detroit NDGPS transmitter is located approximately 1151.7 km from Baxley (GA) in a North-South path and transmits at 319 kHz. The NML transmitter is located approximately 2104.7 km from Baxley (GA) in a more Northwest-Southeast path and transmits at 25.2 kHz. Although the NML-to-Baxley path is not an ideal comparison to the Detroit-to-Baxley path, it can serve as a useful proxy for investigating how the roughness metrics vary with frequency.

First, using the same window and overlap size of 20 ± 2.5 minutes, the horizontal roughness, or correlation length scale, is investigated. Figure 11 summarizes the correlation length scale data for both transmitters. The two left panels show the data for the NDGPS transmitter. The top panel shows the major axis correlation length scale

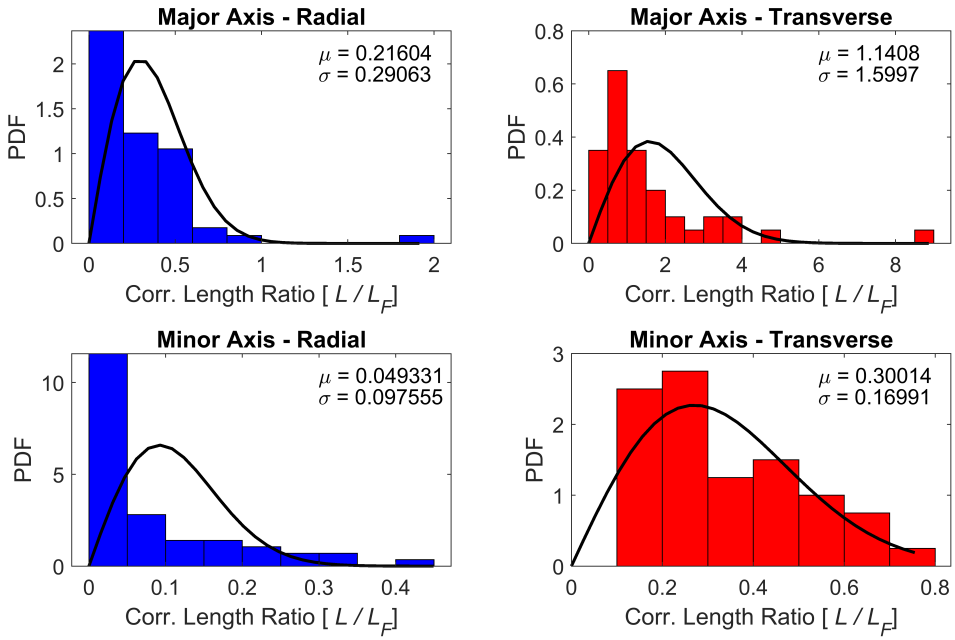

Figure 8. Summary of the measured correlation length scale values for all field campaigns normalized by their approximate Fresnel zone dimensions. Top left panel: Major axis correlation length scale for the radial direction. Top right panel: Major axis correlation length scale for the transverse direction. Bottom left panel: Minor axis correlation length scale for the radial direction. Bottom right panel: Minor axis correlation length scale for the transverse direction.

data and the bottom panel shows the minor axis correlation length scale data. The right panels show the data for the VLF transmitter. The top panel shows the major axis correlation length scale data and the bottom panel shows the minor axis correlation length scale data. Once more, in each panel, the mean, μ, and standard deviation, σ, are show in the top right corner and the black line shows the best fit Rician to give a sense of the shape of the distribution. All values are normalized by the *wavenumber* of the respective transmitter. Between both frequencies, the major and minor axis correlation lengths have similar shapes, but there is a significant difference in the magnitudes of the correlation length values. The NDGPS transmitter values tend to be much higher than the VLF values, primarily due to the correlation length scales being normalized by the wavenumber (i.e. $\propto \frac{1}{\lambda}$) of the transmitters, where VLF wavelengths are about $10\times$ larger than LF/MF wavelengths. The normalization gives a reference for how rough the D-region is given the wavelength and, in general, the correlation length scale can serve as a proxy for the scale of the perturbation, e.g. (Bowles et al., 1963), (Bramley, 1951), and (Lindner, 1975a). In the case of Figure 11, the major axis correlation length scale measured using the NDGPS transmitter is about $8\times$ larger than that measured by the VLF transmitter when normalized by the wavenumber, $3.8\times$ for the minor axis. This suggests that the roughness, or perturbations, measured by the NDGPS transmitters were larger, or caused more angular spreading, relative to the frequency compared to the VLF transmitters. This roughly translates to the D-region electron density being measured as "smoother" when using VLF. Early work using the partial reflection technique, (Lindner, 1975b), found that the angular spreading tended to increase with height. This would be consistent with the trend here if it is assumed that the absolute reflection height of the VLF wave is lower than the LF/MF wave.

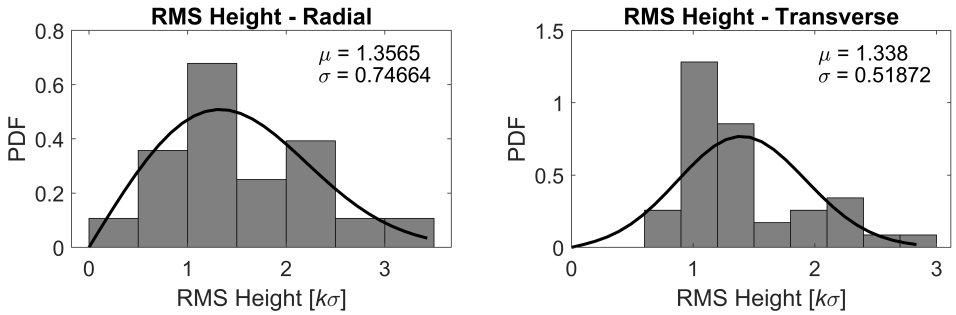

Figure 9. Summary of the RMS height variation values for all field campaigns calculated using the differential phase height method. Left panel: RMS height values calculated for the radial orientation. Right panel: RMS height values calculated for the transverse orientation.

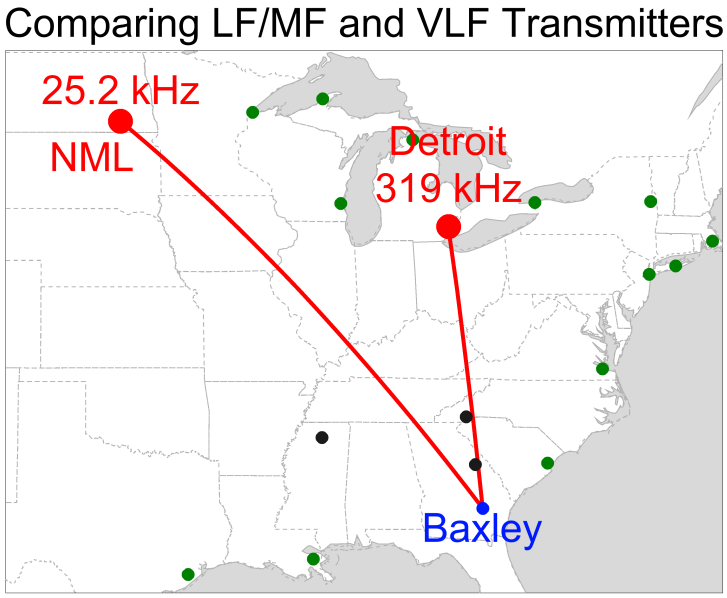

Figure 10. Map of the two transmitter-receiver great circle paths (red lines) used to compare the roughness metrics from a VLF transmitter (NML, 25.2 kHz) and an NDGPS transmitter (Detroit (MI), 319 kHz). Data was collected during the 7-September-2019 field campaign in Baxley, Georgia (blue dot).

Next, using the same window configuration, the vertical roughness, or RMS height variation, is investigated. Figure 12 summarizes the RMS height variation data for both transmitters. The left panel shows the data for the NDGPS transmitter. The right panel shows the data for the VLF transmitter. In each panel, the mean, μ, and standard deviation, σ, are show in the top right corner and the black line shows the best fit Rician to give a sense of the shape of the distribution. All values are normalized by the *wavenumber* of the respective transmitter. Recall that the RMS height variation measured is calculated using the *differential phase height* method described in the previous chapter. Thus, this is a relative measure between two points in the D-region. Both panels have similar shapes, however the left panel mean value, showing the NDGPS transmitter, is about 36× larger than the right right panel, VLF transmitter, mean. This suggests that the variation in phase height between two points is much higher, relatively to a wavelength,

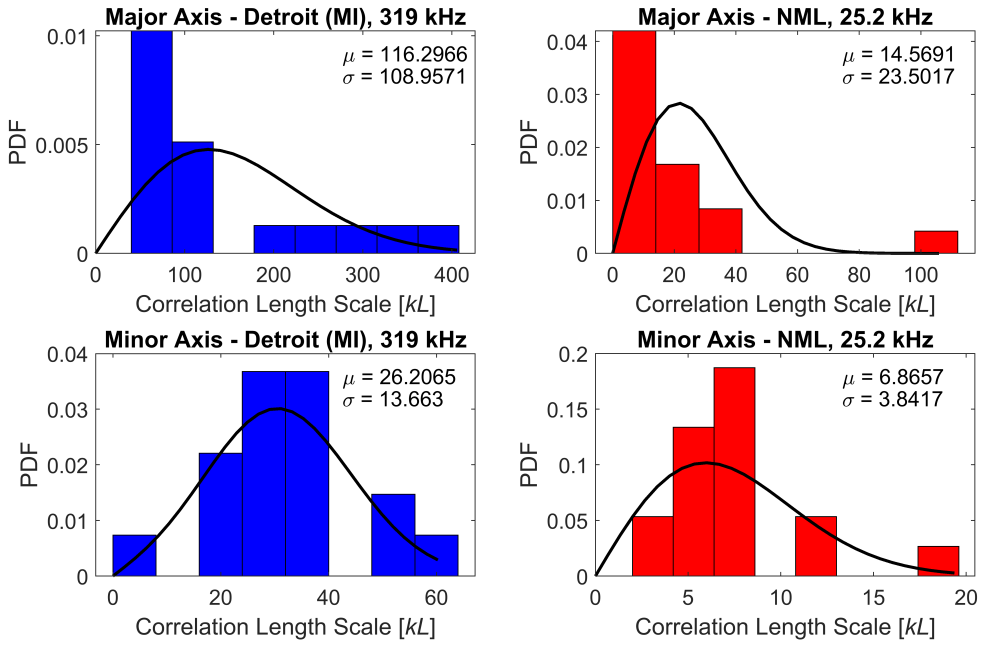

Figure 11. Summary of the correlation length scale values from the 7-September-2019 field campaign calculated in the radial direction. Left panels: Major axis (top) and minor axis (bottom) correlation length scales calculated for the NDGPS transmitter in Detroit (MI) transmitting at 319 kHz at a distance of 1151.7 km. Right panel: Major axis (top) and minor axis (bottom) correlation length scales calculated for the VLF transmitter "NML" transmitting at 25.2 kHz at a distance of 2104.7 km.

for an LF/MF wave than for a VLF wave. This is consistent with the correlation length scale measurement in suggesting that the D-region appears "smoother" for the VLF transmitter.

5 Conclusion

In this paper we present a method of characterizing the horizontal and vertical electron density roughness of the D-region ionosphere using Nationwide Differential GPS (NDGPS) transmitters as Low Frequency (LF; 30−300 kHz) and Medium Frequency (MF; 300−3000 kHz) signals of opportunity. The horizontal roughness is characterized using an amplitude cross-correlation method, which yields the correlation length scale metric. The vertical roughness is characterized using a differential phase height, which is needed to mitigate the effects of transmitter phase instability. The ranges and typical values of roughness metrics are investigated using data from several field campaign measurements. Finally, the roughness metrics for an NDGPS transmitter and VLF transmitter are compared. It is found that the roughness detected by the VLF transmitter is significantly smoother and demonstrates the utility of this method to complement traditional VLF measurements.

Acknowledgments

This work was supported by the National Science Foundation under grant AGS 1451142 and AGS 1653114 (CAREER) to the Georgia Institute of Technology. The first author's

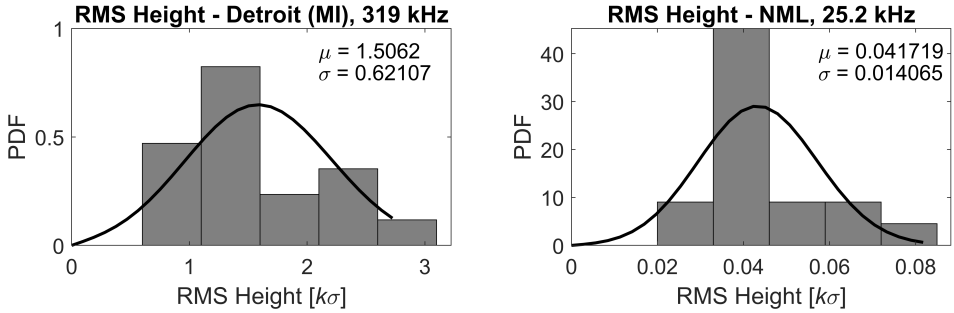

Figure 12. Summary of the RMS height variation values from the 7-September-2019 field campaign calculated using the differential phase height method in the radial direction. Left panel: RMS height values calculated for the NDGPS transmitter in Detroit (MI) transmitting at 319 kHz at a distance of 1151.7 km. Right panel: RMS height values calculated for the VLF transmitter "NML" transmitting at 25.2 kHz at a distance of 2104.7 km.

work was also supported by the NSF Graduate Research Fellowship, DGE 1650044. Data will be made available through the WALDO repository (http://waldo.world/).

References

Arikan, F., & Erol, C. B. (1998). Statistical characterization of time variability in midlatitude single-tone HF channel response. *Radio Science*, *33*(5), 1429–1443. doi: 10.1029/98RS01889

Belrose, J., Hatton, W., McKerrow, C., & Thain, R. (1959, may). The Engineering of Communication Systems for Low Radio Frequencies. *Proceedings of the IRE*, *47*(5), 661–680. Retrieved from `http://ieeexplore.ieee.org/document/4065729/` doi: 10.1109/JRPROC.1959.287236

Belrose, J., & Thomas, L. (1968, jan). Ionization changes in the middle latitude D-region associated with geomagnetic storms. *Journal of Atmospheric and Terrestrial Physics*, *30*(7), 1397–1413. Retrieved from `https://www.sciencedirect.com/science/article/pii/S0021916968912609` doi: 10.1016/S0021-9169(68)91260-9

Bickel, J. E. (1957, sep). A method for obtaining LF oblique-incidence reflection coefficients and its application to 135.6-kc/s data in the Alaskan area. *Journal of Geophysical Research*, *62*(3), 373–381. Retrieved from `http://doi.wiley.com/10.1029/JZ062i003p00373` doi: 10.1029/JZ062i003p00373

Bowles, K. L., Balsley, B. B., & Cohen, R. (1963, may). Field-aligned E -region irregularities identified with acoustic plasma waves. *Journal of Geophysical Research*, *68*(9), 2485–2501. doi: 10.1029/jz068i009p02485

Bramley, E. (1951, jan). Diversity effects in spaced-aerial reception of ionospheric waves. *Proceedings of the IEE - Part III: Radio and Communication Engineering*, *98*(51), 19–25. Retrieved from `https://digital-library.theiet.org/content/journals/10.1049/pi-3.1951.0004` doi: 10.1049/pi-3.1951.0004

Briggs, B. H., Phillips, G. J., & Shinn, D. H. (1950). The analysis of observations on spaced receivers of the fading of radio signals. *Proceedings of the Physical Society. Section B*, *63*(2), 106–121. doi: 10.1088/0370-1301/63/2/305

Clarke, C. (1962). Atmospheric radio-noise studies based on amplitude-probability measurements at Slough, England, during the International Geophysical Year. *Proceedings of the IEE Part B: Electronic and Communication Engineering*, *109*(47), 393. Retrieved from `http://digital-library`

.theiet.org/content/journals/10.1049/pi-b-2.1962.0224 doi: 10.1049/pi-b-2.1962.0224

Cohen, M. B., Said, R. K., Paschal, E. W., McCormick, J. C., Gross, N. C., Thompson, L., ... Chang, J. (2018, sep). Broadband longwave radio remote sensing instrumentation. *Review of Scientific Instruments*, *89*(9), 094501. Retrieved from http://aip.scitation.org/doi/10.1063/1.5041419 doi: 10.1063/1.5041419

Doviak, J., Lataitis, J., Holloway, L., & Van Baelen, J. (1994). A Generalized Theoretical Analysis of Cross-correlation and Cross-spectra for Spaced-antenna Wind Profilers. doi: 10.5065/D6N014G4

Doviak, R. J., & Zrnic, D. S. (1983). Fresnel zone considerations for reflection and scatter from refractive index irregularities. In *Conference on radar meteorology of the american meteorological society* (pp. 111–117). Retrieved from https://ntrs.nasa.gov/search.jsp?R=19840019023

Durgin, G. (2002). Space-Time Wireless Channels. *Space-Time Wireless Channels*, 1–19. Retrieved from https://books.google.com/books?hl=en{\&}lr={\&}id=6sK3nYBoUmAC{\&}oi=fnd{\&}pg=PR15{\&}dq=space-time+wireless+channels+durgin{\&}ots=BN6cL53cgX{\&}sig=P{_}6I2rPJjzyIBJCfMraAWHucPcshttp://www.ncbi.nlm.nih.gov/pubmed/23834000 doi: 10.1300/J155v04n04_01

Füllekrug, M., Koh, K., Liu, Z., & Mezentsev, A. (2019, jan). First Map of Coherent Low-Frequency Continuum Radiation in the Sky. *Radio Science*, *54*(1), 44–59. Retrieved from http://doi.wiley.com/10.1029/2018RS006705 doi: 10.1029/2018RS006705

Füllekrug, M., Smith, N., Mezentsev, A., Watson, R., Astin, I., Gaffet, S., ... Rycroft, M. (2015, nov). Multipath propagation of low-frequency radio waves inferred from high-resolution array analysis. *Radio Science*, *50*(11), 1141–1149. Retrieved from http://doi.wiley.com/10.1002/2015RS005781 doi: 10.1002/2015RS005781

Gross, N. C., Cohen, M. B., Said, R. K., & Gołkowski, M. (2018, jan). Polarization of Narrowband VLF Transmitter Signals as an Ionospheric Diagnostic. *Journal of Geophysical Research: Space Physics*, *123*(1), 901–917. Retrieved from http://doi.wiley.com/10.1002/2017JA024907 doi: 10.1002/2017JA024907

Higginson-Rollins, M. A., & Cohen, M. B. (2017, aug). Exploiting LF/MF signals of opportunity for lower ionospheric remote sensing. *Geophysical Research Letters*, *44*(16), 8665–8671. Retrieved from http://doi.wiley.com/10.1002/2017GL074236 doi: 10.1002/2017GL074236

Higginson-Rollins, M. A., & Cohen, M. B. (2020). Studying the Effects of the August 2017 Solar Eclipse using LF/MF Signals of Opportunity. doi: 10.1002/ESSOAR.10502560.1

Hocking, W. (1987, nov). Reduction of the effects of non-stationarity in studies of amplitude statistics of radio wave backscatter. *Journal of Atmospheric and Terrestrial Physics*, *49*(11-12), 1119–1131. Retrieved from https://www.sciencedirect.com/science/article/pii/0021916987900948 doi: 10.1016/0021-9169(87)90094-8

Hocking, W. K. (1979). Angular and temporal characteristics of partial reflections from the D-region of the ionosphere. *Journal of Geophysical Research*, *84*(A3), 845. doi: 10.1029/ja084ia03p00845

Kotovsky, D. A., & Moore, R. C. (2016, may). Photochemical response of the nighttime mesosphere to electric field heating-Onset of electron density enhancements. *Journal of Geophysical Research: Space Physics*, *121*(5), 4782–4799. Retrieved from http://doi.wiley.com/10.1002/2015JA022054 doi: 10.1002/2015JA022054

Last, D., & Poppe, D. (1996, dec). A Coverage Prediction Model for Radio Beacon Differential Satellite Navigation Systems. *Navigation*, *43*(4), 451–469. Retrieved from http://doi.wiley.com/10.1002/j.2161-4296.1996.tb01932.x doi: 10.1002/j.2161-4296.1996.tb01932.x

Last, J., & Poppe, D. (1997). Effect of skywave interference on coverage of radiobeacon DGPS stations. *IEE Proceedings - Radar, Sonar and Navigation*, *144*(3), 163. Retrieved from http://digital-library.theiet.org/content/journals/10.1049/ip-rsn{_}19971177 doi: 10.1049/ip-rsn:19971177

Lay, E. H., & Shao, X. M. (2011a, jan). High temporal and spatial - resolution detection of D - layer fluctuations by using time - domain lightning waveforms. *Journal of Geophysical Research: Space Physics*, *116*(January), 1–8. Retrieved from http://doi.wiley.com/10.1029/2010JA016018 doi: 10.1029/2010JA016018

Lay, E. H., & Shao, X. M. (2011b, dec). Multi-station probing of thunderstorm-generated D-layer fluctuations by using time-domain lightning waveforms. *Geophysical Research Letters*, *38*(23), n/a–n/a. Retrieved from http://doi.wiley.com/10.1029/2011GL049790 doi: 10.1029/2011GL049790

Lindner, B. (1975a). The Nature of D-region Scattering of Vertical Incidence Radio Waves. I. Generalized Statistical Theory of Diversity Effects Between Spaced Receiving Antennas. *Australian Journal of Physics*, *28*(2), 163. Retrieved from http://www.publish.csiro.au/?paper=PH750163 doi: 10.1071/PH750163

Lindner, B. (1975b). The Nature of D-region Scattering of Vertical Incidence Radio Waves. II. Experimental Observations Using Spaced Antenna Reception. *Australian Journal of Physics*, *28*(2), 171. Retrieved from http://www.publish.csiro.au/?paper=PH750171 doi: 10.1071/PH750171

Mathews, J. D., Shapiro, J. H., & Tanenbaum, B. S. (1973, dec). Evidence for distributed scattering in D region partial-reflection processes. *Journal of Geophysical Research*, *78*(34), 8266–8275. Retrieved from http://doi.wiley.com/10.1029/JA078i034p08266 doi: 10.1029/JA078i034p08266

McCormick, J. C., Cohen, M. B., Gross, N. C., & Said, R. K. (2018, apr). Spatial and Temporal Ionospheric Monitoring Using Broadband Sferic Measurements. *Journal of Geophysical Research: Space Physics*, *123*(4), 3111–3130. Retrieved from http://doi.wiley.com/10.1002/2017JA024291 doi: 10.1002/2017JA024291

McKerrow, C. (1957). Some Recent Measurements of Atmospheric Noise in Canada. *Proceedings of the IRE*, *45*(6), 782–786. Retrieved from http://ieeexplore.ieee.org/document/4056602/ doi: 10.1109/JRPROC.1957.278475

McKerrow, C. A. (1960, jul). Some measurements of atmospheric noise levels at low and very low frequencies in Canada. *Journal of Geophysical Research*, *65*(7), 1911–1926. Retrieved from http://doi.wiley.com/10.1029/JZ065i007p01911 doi: 10.1029/JZ065i007p01911

Nicolet, M., & Aikin, A. C. (1960, may). The formation of the D region of the ionosphere. *Journal of Geophysical Research*, *65*(5), 1469–1483. Retrieved from http://doi.wiley.com/10.1029/JZ065i005p01469 doi: 10.1029/JZ065i005p01469

P. Beckmann, & A. Spizzichino. (1963). *The Scattering of Electromagnetic Waves from Rough Surfaces*. New York: Pergamon Press.

Piggott, W. R., Pitteway, M. L. V., & Thrane, E. V. (1965, mar). The Numerical Calculation of Wave-Fields, Reflexion Coefficients and Polarizations for Long Radio Waves in the Lower Ionosphere. II. *Philosophical Transactions of the Royal Society A: Mathematical, Physical and Engineering Sciences*, *257*(1079), 243–271. doi: 10.1098/rsta.1965.0005

Ratcliffe, J. A. (1956). Some aspects of diffraction theory and their application to the ionosphere. *Reports on Progress in Physics*, *19*(1), 188–267. doi: 10.1088/0034-4885/19/1/306

Shapiro, J. H. (1973, may). Statistical models for D-region partial-reflection experiments. *Radio Science*, *8*(5), 431–435. Retrieved from http://doi.wiley.com/10.1029/RS008i005p00431 doi: 10.1029/RS008i005p00431

Spetzler, J., Sivaji, C., Nishizawa, O., & Fukushima, Y. (2002). A test of ray theory and scattering theory based on a laboratory experiment using ultrasonic waves and numerical simulation by finite-difference method. *Geophysical Journal International*, *148*(2), 165–178. Retrieved from https://academic.oup.com/gji/article-abstract/148/2/165/596588 doi: 10.1046/j.1365-246X.2002.01552.x

Spetzler, J., & Snieder, R. (2001a). The effect of small-scale heterogeneity on the arrival time of waves. *Geophysical Journal International*, *145*(3), 786–796. Retrieved from https://academic.oup.com/gji/article-abstract/145/3/786/648126 doi: 10.1046/j.1365-246X.2001.01438.x

Spetzler, J., & Snieder, R. (2001b). The formation of caustics in two-and three-dimensional media. *Geophysical Journal International*, *144*(1), 175–182. Retrieved from https://academic.oup.com/gji/article-abstract/144/1/175/764650 doi: 10.1046/j.1365-246X.2001.00308.x

Thomson, N. R., Clilverd, M. A., & McRae, W. M. (2007, jul). Nighttime ionospheric D region parameters from VLF phase and amplitude. *Journal of Geophysical Research: Space Physics*, *112*(7), n/a–n/a. Retrieved from http://doi.wiley.com/10.1029/2007JA012271 doi: 10.1029/2007JA012271

Wernik, A. W., Liu, C. H., & Yeh, K. C. (1983). Modeling of spaced-receiver scintillation measurements. *Radio Science*, *18*(5), 743–764. doi: 10.1029/RS018i005p00743

Wolfe, D. B., Judy, C. L., Haukkala, E. J., & Godfrey, D. J. (2000). Engineering The World's Largest DGPS Network. *Control Engineering*, *1*(June), 26–28. Retrieved from http://ieeexplore.ieee.org/document/881237/ doi: 10.1109/OCEANS.2000.881237